Effect of electron radiation on small-signal parameters of NMOS devices at mm-wave frequencies

Brilliant Habeenzu[a*], Walter Meyer [b], Tinus Stander [a]

[a] Carl & Emily Fuchs Institute for Microelectronics, Department of Electrical, Electronic & Computer Engineering, University of Pretoria, Pretoria 0002, SOUTH AFRICA
[b] Department of Physics, University of Pretoria, Pretoria 0002, SOUTH AFRICA

A R T I C LE I N FO

Keywords:
CMOS technology, integrated circuit modelling, parameter extraction, total ionizing dose.

ABSTRACT

The effect of electron radiation on the forward-active small-signal model parameters for 0.35 µm CMOS devices are reported. Four devices with different gate widths were exposed to electron radiation using a Strontium 90 (Sr 90) radiation source at dose rates of 200 kRad (Si)/hr up to a total radiation dose of 2.7 MRad. S-parameters were measured, and small-signal models extracted, both pre-irradiation and at regular dose intervals. Relationships between small-signal model parameters and total radiation dose d were derived and used to calculate small-signal parameters. The major model variations due to total ionizing dose exposure were increases in the gate resistance (R_g), gate drain capacitance (C_{gd}) and gate source capacitance (C_{gs}), with a reduction in transconductances (g_m and g_{ds}). This results in S_{11} and S_{22} becoming more resistive as d is increased, with a decrease in the unilateral gain, f_T and f_{max}. The application of the data in predictive modelling of radiation damage is demonstrated.

1. Introduction

The availability of the unlicensed and lightly licensed spectrum in the mm-wave frequency bands have led to increased research in mm-waves applications in space [1]. The RF performance of CMOS devices have improved such that bulk CMOS is now a viable technology for high frequency designs that have historically been dominated by high speed silicon bipolar and III–V technologies [2], As a result of this, bulk CMOS is increasingly being adopted for RF applications in radiation prone environments [3],[4], making it increasingly important to understand and predict the radiation degradation CMOS devices [5]-[6] at high frequencies.

Substantial work has been done in linear, small-signal circuit modelling of bulk CMOS devices [7],[8]. These methods establish nominal model parameters from measurement, but do not account for device degradation due to ionizing radiation. This shortcoming may lead to inaccurate estimations of circuit and system performance over the circuit's operating lifetime.

In this work, we derive relationships between total ionizing dose (TID) due to electron radiation, and the forward active small-signal model parameters of four bulk NMOS devices prototyped in the ams C35 0.35 µm CMOS process [9]. Models are extracted at five incremental doses, and compared

* Corresponding author
E-mail address: brilliant.habeenzu@tuks.co.za (B. Habeenzu)

to linear RF measurement results up to 50 GHz. The model's efficacy at predicting small-signal performance degradation for a given dose is subsequently evaluated.

The paper is organized as follows:

Section 2 presents the devices under test, and well as the radiation and microwave measurement equipment and procedures. The NMOS small-signal model selected for this experiment is discussed in Section 3, along with the procedure to generate model values from S-parameter measurements. The results of the extraction are presented in Section 4, (both as the extracted model parameters and the derived relationships to radiation dose *d*,) and the relationship validated using measured data. The derived relationships are then applied in Section 5 to predict the performance of an irradiated device, after which concluding remarks are presented in Section 6.

2. Material and Methods

2.1.Devices under test

To compare the effect of radiation on the size of the gate, four NMOS devices (Fig. 3) with gate widths of 1×5 µm, 5×5 µm, 1×10 µm and 5×10 µm were selected, to evaluate the effect of gate width on TID damage as well. The devices were drawn in common source configuration with the substrate tied to the source and grounded. Model simulations in Cadence Spectre RF were used to determine the bias conditions for maximum f_T and the resulting linear dynamic range. The selected bias conditions are shown in Table I, which all resulted in P1db values of above +10 dBm. A die micrograph is shown in Fig. 1.

Table 1: Bias conditions for NMOS devices

Total gate width (µm)	V_{GS}	V_{DS}	I_D (mA)
5	2.08 V	3.5 V	1.3
10	2.03 V	3.5 V	2.6
25	2.10 V	3.5 V	6.6
50	2.03 V	3.5 V	13.2

2.2.Electron radiation setup

A test method which uses electron radiation from a Strontium 90 (Sr-90) lab source was adopted**.** The prescribed method requires an electron accelerator source, which would be collimated and monochromatic, while the electrons from the Sr-90 source are not collimated and range from 0 to ≈ 2.2 MeV. The radiation is emitted in two peaks, one with energy ranging from 0 to ≈ 500 keV (average 200 keV) due to Sr-90, and the second with energy ranging from 0 to 2.28 MeV (average 940 keV) due to Yt-90 decay [10]. Since the stopping power of silicon for electrons varies by less than 50% over the range 100 eV to 40 MeV [11], the results are expected to agree qualitatively (if not quantitatively) to those produced by ESCC 22900. Using the known source activity of 3.1 GBq, the separation distance between the radiation source and the DUT was set up at 0.4 cm as shown in Fig. 2 such that the radiation dose rate was 200 kRad (Si)/hr. This radiation dose rate was chosen to be within the range of dose rates in the "standard" window defined in ESCC 22900, with further consideration to the targeted total dose and radiation safety.

The experiment was executed as a remote testing experiment in which radiation exposure was completed in a separate facility from where RF measurements were conducted. The transistors were irradiated in an unbiased condition with terminals floating as applied in [12] for AC measurements. The devices were removed from radiation for characterization, and returned for continued radiation, within an hour, to limit the effect of possible room temperature annealing [13]. Due to a limited availability of devices under test, only one device of each size was considered. Although more samples

would be required to validate the exact fitting curves and calculate error bounds, the selection of four devices is expected to demonstrate qualitative agreement in degradation. The radiation exposure periods and accumulated TID dose *d* are listed in Table 2.

Table 2: Dose rate and cumulative d in radiation experiment

Experiment No.	Dose rate (kRad(Si)/hr)	Cumulative d (kRad)
1	200	200
2	200	690
3	200	1300
4	200	2000
5	200	2700

2.3.Determination of the dose rate

The dose rate delivered by the Sr-90 source to the device was determined by placing Ashland Gafchromic EBT3 film[14] at the same position as the device and exposing it to radiation for 5, 10, 15, 20, 25 and 30 s as shown in Fig. 2(b). Timings were confirmed by analysing video recording of the procedure. For reference, a further two pieces of Gafchromic EBT3 film were exposed to 4 MeV electrons to a dose of 500 and 1000 rad(H_2O) using an Elekta Synergy Platform radiotherapy system, which was in clinical use and with valid calibration. The Gafchromic EBT3 film was analysed using the Ashland FilmQA Pro (2016) using an Epson Perfection 2400 48 bit color scanner at 200 dpi and using the color reciprocal linear vs dose calibration curve. Precautions as described in the user manual were taken, and care was taken to ensure that the measured regions were centred horizontally on the scanner. Initially, a tentative calibration curve was determined using an assumed dose rate for the Sr-90 irradiation. This assumed calibration curve was then used to determine the dose received by the reference samples. The assumed dose rate was then varied until the dose rate obtained for the reference samples corresponded most closely to the dose delivered by the radiotherapy system. Using this procedure, a dose rate of 230 krad/h (H_2O) was obtained for irradiation by the Sr-90 source, which corresponds to 200 krad/h (Si) assuming 1 MeV electrons and stopping powers as provided by the ESTAR database [11].

2.4.Linear measurements

S-parameters were measured on an Anritsu ME7828A vector network analyzer (VNA) from 1 to 50 GHz through GSG wafer probing, with bias tees providing DC biasing at the source and the gate (Fig. 4). First-tier calibration used the LRM method to shift the calibration plane to the probe tips using calibration standards from the ceramic ISS. S-parameters measurements on the four NMOS devices were then second-tier de-embedded using TRL standards on-chip as part of the model extraction process.

3. Theory

In this work, the small-signal model for a MOSFET presented in [8] has been adopted, with some modifications. The changes include the removal of two current sources from the circuit. Since the devices in this study have the substrate and the source tied together and connected in common source configuration, the substrate, to source voltage (V_{bs}) is 0. It therefore follows that the voltage controlled current source, which depends on V_{bs}, becomes an open circuit. Similarly, the current source which is dependent on the derivative of V_g with respect to time has been converted to an open circuit, as the gate voltage (V_g) is constant, resulting in a derivative of 0. This leaves the adopted model with only one voltage controlled current source, as shown in Fig. 4. To extract small-signal parameters, the measured S-parameters were first de-embedded using the TRL method presented in [15] and converted to Y-parameters. Small-signal parameters were then extracted from the Y-parameters using the

method outlined in [8]. The process was repeated after each incremental dose of TID.

4. Results and discussion

4.1.Extracted parameter data

Small-signal parameters were extracted at incremental TID levels using the method outlined in Section 3. The extracted small-signal parameters are indicated in Tables 3 - 6. The data show that the resistance and capacitance values generally increase as d increases whereas g_m reduces with increase in d. This trends can be attributed to the manner in which ionizing radiation damages the semiconductor-dielectric interface, which leads to an increase in effective charge and higher effective capacitance [16]. Ionizing radiation can further damage bulk CMOS devices by striking an electron in the valence band, causing it to gain energy and join the conduction band. This leads to the production of an electron hole pair which may drift under the effect of an electric field towards the gate oxide layer as trapped charges. The trapped charges can shift the threshold voltage, increasing R_g and reducing g_m. Trapped charges can further cause a reduction in the mobility of the device and an increase in the surface resistivity in the lightly doped drain [17],[18]. An increase in the surface resistivity of the drain leads to an increase in R_{ds} and R_{bb}. Furthermore, ionizing radiation can generate oxide and interface traps leading to an increase in the oxide and interface trap charge densities. This can cause structural modification in the material, increasing the dielectric constant, and eventually increasing the gate oxide capacitance (C_{gs} and C_{gd}) and the drain source interface capacitance (C_{db}, C_{bb}, and C_{sd}) as indicated in [19]. To evaluate the accuracy of the extracted small-signal parameters in Tables 3 to 6 and validate the model, circuit simulations were compared to VNA measurements in Fig. 6 to Fig. 9. It is found that there is generally a good agreement between the measured and circuit simulated responses pre-radiation up to 22 GHz.

Table 3: Extracted model parameters for w = 5 μm

Parameter	Pre-rad	200 kRad	690 kRad	1.3 MRad	2 MRad	2.7 MRad
R_g(Ω)	19.91	21.93	22.66	23.84	24.92	25.68
C_{gd}(fF)	2.78	2.85	2.96	3.14	3.39	3.55
C_{gs}(fF)	50.50	52.88	55.61	57.50	59.61	60.98
g_m(mS)	1.1001	1.0998	1.0993	1.0989	1.0987	1.0984
R_{ds}(Ω)	848.82	852.68	853.99	855.02	857.16	858.96
C_{sd}(fF)	15.56	16.39	16.90	17.57	18.98	21.00
C_{db}(fF)	41.04	42.67	43.35	44.97	46.02	48.88
C_{bb}(fF)	135.27	136.68	138.98	140.12	142.78	143.64
R_{bb}(Ω)	14.77	15.69	16.99	18.67	21.35	24.01

Table 4: Extracted model parameters for w = 10 μm

Parameter	Pre-rad	200 kRad	690 kRad	1.3 MRad	2 MRad	2.7 MRad
R_g(Ω)	23.74	25.08	26.13	27.04	28.72	29.30
C_{gd}(fF)	3.49	3.60	3.69	3.75	3.82	3.99
C_{gs}(fF)	54.04	54.47	55.27	56.14	57.24	58.03
g_m(mS)	2.1011	2.1009	2.1006	2.1004	2.1001	2.1000
R_{ds}(Ω)	748.60	750.88	752.09	753.96	755.09	756.75
C_{sd}(fF)	23.85	24.25	25.05	26.28	27.32	28.66
C_{db}(fF)	44.68	45.99	46.99	47.35	48.37	49.10
C_{bb}(fF)	132.85	133.61	134.78	135.49	136.76	137.98
R_{bb}(Ω)	29.84	30.03	30.97	31.18	31.67	32.07

Table 5: Extracted model parameters for w = 25 μm

Parameter	Pre-rad	200 kRad	690 kRad	1.3 MRad	2 MRad	2.7 MRad
$R_g(\Omega)$	16.84	17.15	18.00	18.35	19.25	20.01
C_{gd}(fF)	4.67	4.82	5.00	5.42	5.67	5.93
C_{gs}(fF)	79.80	80.31	81.82	83.88	84.01	86.29
g_m(mS)	5.900	5.895	5.893	5.889	5.886	5.882
$R_{ds}(\Omega)$	616.62	629.64	648.94	674.15	693.38	712.08
C_{sd}(fF)	21.92	23.77	25.75	28.67	31.99	35.01
C_{db}(fF)	51.74	53.03	56.97	58.01	62.88	66.99
C_{bb}(fF)	59.14	100.60	129.42	143.16	158.64	164.94
$R_{bb}(\Omega)$	34.89	36.77	39.07	40.85	42.06	44.19

Table 6: Extracted model parameters for w = 50 μm

Parameter	Pre-rad	200 kRad	690 kRad	1.3 MRad	2 MRad	2.7 MRad
$R_g(\Omega)$	38.60	41.52	48.47	58.70	69.27	80.26
C_{gd}(fF)	14.78	16.01	18.82	20.47	22.29	24.19
C_{gs}(fF)	100.46	102.16	106.95	109.16	112.79	115.80
g_m(mS)	12.60	12.50	12.30	12.10	11.89	11.49
$R_{ds}(\Omega)$	619.43	647.51	670.92	699.26	715.18	736.28
C_{sd}(fF)	45.84	46.93	48.22	52.99	54.09	57.86
C_{db}(fF)	64.92	65.13	67.01	69.55	71.32	74.00
C_{bb}(fF)	90.81	94.13	98.92	103.02	107.31	113.42
$R_{bb}(\Omega)$	74.58	76.22	77.91	79.02	80.35	82.00

4.2.Regression

The extracted small-signal parameters in Tables 3 to 6were used in curve fitting tool to derive equations relating changes in the small-signal model and the substrate parameters to *d*. The derived equations are shown in Tables 7 to 10.

Table 7: Derived relationships for w = 5 μm

Parameter	Derived equations	R^2
$R_g(\Omega)$	$R_g = 21.87e^{0.0000618d} - 1.96e^{-0.01101d}$	0.9957
C_{gd}(fF)	$C_{gd} = 2.789e^{0.00009166d}$	0.9957
C_{gs}(fF)	$C_{gs} = 54.66e^{0.00004142d} - 4.133e^{-0.002898d}$	0.9988
g_m(mS)	$g_m = 1.099e^{-0.0000001368d} + 0.001333e^{-0.0009952d}$	0.9967
$R_{ds}(\Omega)$	$R_{ds} = 852.2e^{0.0000029d} - 3.467e^{-0.003311d}$	0.9948
C_{sd}(fF)	$C_{sd} = 15.83e^{0.0000848d} + 0.0009674e^{0.00216d}$	0.9904
C_{db}(fF)	$C_{db} = 41.91e^{0.00005361d} - 0.8757e^{-0.1044d}$	0.9807
C_{bb}(fF)	$C_{bb} = 137.7e^{0.00001629d} - 2.424e^{-0.002569d}$	0.9899
$R_{bb}(\Omega)$	$R_{bb} = 14.96e^{0.0001761d}$	0.9983

Table 8: Derived relationships for w = 10 μm

Parameter	Derived equation	R^2
$R_g(\Omega)$	$R_g = 25.15e^{0.00005944d} - 1.411e^{-0.006605d}$	0.9903
C_{gd}(fF)	$C_{gd} = 3.568e^{0.00003886d} - 0.08499e^{-0.005147d}$	0.9839
C_{gs}(fF)	$C_{gs} = 54.18e^{0.00002642d}$	0.9945
g_m(mS)	$g_m = 2.101e^{-0.0000001515d} + 0.0003053e^{-0.003639d}$	0.9920
$R_{ds}(\Omega)$	$R_{ds} = 750.7e^{0.000002973d} + 2.138e^{-0.009787d}$	0.9965
C_{sd}(fF)	$C_{sd} = 23.92e^{0.00006751d}$	0.9979
C_{db}(fF)	$C_{db} = 46.14e^{0.00002301d} - 1.462e^{-0.007074d}$	0.9956
C_{bb}(fF)	$C_{bb} = 133.5e^{0.000012d} - 0.6985e^{-0.005684d}$	0.9974

$R_{bb}(\Omega)$	$R_{bb} = 30.69e^{0.00001609d} - 0.9218e^{-0.001998d}$	0.9844

Table 9: Derived relationships for w = 25 μm

Parameter	Derived equation	R^2
$R_g(\Omega)$	$R_g = 17.2e^{0.00005586d} - 0.3786e^{-0.003768d}$	0.9934
C_{gd}(fF)	$C_{gd} = 4.73e^{0.00008804d}$	0.9818
C_{gs}(fF)	$C_{gs} = 81.13e^{0.000021816d} - 1.432e^{-0.001714d}$	0.9703
g_m(mS)	$g_m = 5.896e^{-0.0000009062d} + 0.003664e^{-0.01661d}$	0.9974
$R_{ds}(\Omega)$	$R_{ds} = 664.2e^{0.00002862d} - 46.83e^{-0.0008055d}$	0.9989
C_{sd}(fF)	$C_{sd} = 23.45e^{0.000151d} - 1.517e^{-0.006214d}$	0.9985
C_{db}(fF)	$C_{db} = 52.72e^{0.00008784d} - 1.03e^{-0.005158d}$	0.9865
C_{bb}(fF)	$C_{bb} = 125e^{0.0001076d} - 65.63e^{-0.00428d}$	0.9973
$R_{bb}(\Omega)$	$R_{bb} = 37.82e^{0.0000567d} - 2.939e^{-0.003495d}$	0.9977

-

Table 10: Derived relationships for w= 50 μm

Parameter	Derived equation	R^2
$R_g(\Omega)$	$R_g = 40.04e^{0.0002642d}$	0.9918
C_{gd}(fF)	$C_{gd} = 18.05e^{0.0001083d} - 3.357e^{-0.00202d}$	0.9985
C_{gs}(fF)	$C_{gs} = 104.5e^{0.00003815d} - 4.204e^{-0.002248d}$	0.9959
g_m(mS)	$g_m = 12.6e^{-0.00003233d}$	0.9869
$R_{ds}(\Omega)$	$R_{ds} = 659.4e^{0.00004122d} - 39.28e^{-0.003559d}$	0.9961
C_{sd}(fF)	$C_{sd} = 46.08e^{0.00008536d}$	0.9724
C_{db}(fF)	$C_{db} = 64.79e^{0.00004949d}$	0.9931
C_{bb}(fF)	$C_{bb} = 94.31e^{0.00006744d} - 3.528e^{-0.004707d}$	0.9833
$R_{bb}(\Omega)$	$R_{bb} = 76.5e^{0.00002539d} - 1.93e^{-0.005495d}$	0.9989

It is evident that all the coefficient of determination (R^2) values are above 0.97, indicating that the derived regression curves fit the data well. To evaluate the efficacy of the regression approach, model parameters calculated at 690 kRad were compared to the values extracted from measurement at 690 kRad. The comparison in Table 11 indicates that the values obtained by extraction from S-parameters, and those obtained by regression, agree well.

Table 11: Comparison of calculated parameters to parameters extracted from measurements at 690 kRad

Parameter	w = 5 μm		w = 10 μm		w = 25 μm		w = 50 μm	
	Regression	Measured	Regression	Measured	Regression	Measured	Regression	Measured
$R_g(\Omega)$	22.5	22.6	26.14	26.13	17.82	17.99	48.05	48.20
C_{gd}(fF)	2.95	2.96	3.66	3.66	5.04	4.92	18.62	18.08
C_{gs}(fF)	55.24	55.17	55.4	55.6	81.86	81.82	106.40	106.95
g_m(mS)	1.10	1.10	2.10	2.10	5.89	5.89	12.32	12.99
$R_{ds}(\Omega)$	853.45	853.99	752.46	752.09	673.98	673.78	649.92	649.94
C_{sd}(fF)	16.76	16.80	25.06	25.05	25.34	25.35	49.07	49.10
C_{db}(fF)	43.90	43.40	46.84	46.90	55.85	55.87	67.04	67.11
C_{bb}(fF)	138.82	138.87	134.57	134.56	58.83	58.84	98.67	98.52
$R_{bb}(\Omega)$	39.07	39.07	30.79	30.97	130.60	129.42	77.81	77.52

4.3.Application of model

To demonstrate the usage of the extracted model, small-signal parameter values were calculated using the derived relationships at a *d* of 6.25 MRad, at which the values of the small-signal parameters were not measured. The calculated values of the small-signal parameters at *d* of 6.25 MRad are shown in Table 12.

Table 12: Calculated parameters at 6.25 MRad

Parameter	w=5 µm	w=10 µm	w=25 µm	w=50 µm
$R_g(\Omega)$	32.18	36.47	24.39	208.75
C_{gd}(fF)	4.55	4.95	8.20	35.52
C_{gs}(fF)	63.91	70.81	92.98	132.64
g_m(mS)	1.091	2.099	5.863	10.295
$R_{ds}(\Omega)$	867.79	764.78	793.99	853.17
C_{sd}(fF)	32.53	36.48	60.29	71.56
C_{db}(fF)	58.59	53.28	91.29	88.28
C_{bb}(fF)	152.46	143.90	244.89	143.75
$R_{bb}(\Omega)$	44.97	33.94	53.90	89.66

4.4.Predicted S-parameter variation

S-parameters were obtained from circuit simulation using the calculated small-signal parameters at d of 6.25 MRad, and compared to results pre-radiation. The S_{21} responses in Fig. 10 to Fig. 13 would indicate substantial change to the gain of all four devices, while the Smith charts in Figs. 14 to 17 would indicate that the device is expected to become progressively more resistive at the gate input, which is exacerbated in large gate width devices. This is consistent with previous findings [17] that smaller devices are less susceptible to TID damage. On the contrary, the output impedance is expected to remain largely unaffected by TID, as is evident from Figs. 18 to 21. This would indicate that the input impedance matching to a small-signal RF amplifier would be more affected by TID damage than the output matching.

4.5.Unilateral power gain and current gain

The impact of TID on the performance of the transistors was further evaluated using the unilateral gain (U) [12] in Fig. 22 to Fig. 25, as well as current gain of $|A_i|$ in Fig. 26 to Fig. 29. It is evident that increased dose leads to lower gain in both regards; moreover, it is evident that the extracted model parameter relationships can be used to predict these values at extrapolated TID levels.

4.6.Effect on f_T and f_{max}

As can be seen from the decreased 0 dB intercepts of $|A_i|$ and U, increased d results in both lower f_T and f_{max}. These results are tabulated in Tables 13 and 14, further illustrating the value of the predictive approach.

Table 13: Cut off frequency values

Radiation dose (d)	w=5 µm	w=10 µm	w=25 µm	w=50 µm
Pre rad	3.3 GHz	5.9 GHz	10.1 GHz	14.7 GHz
200 kRad	3.2 GHz	5.5 GHz	9.7 GHz	14.4 GHz
690 kRad	3.0 GHz	5.3 GHz	8.9 GHz	13.2 GHz
1.3 MRad	2.9 GHz	5.2 GHz	8.3 GHz	12.7 GHz
2 MRad	2.8 GHz	5.0 GHz	7.9 GHz	12.0 GHz
2.7 MRad	2.7 GHz	4.9 GHz	7.0 GHz	11.3 GHz
6.25 MRad	2.2 GHz	4.8 GHz	5.1 GHz	6.50 GHz

Table 14: Maximum oscillation frequency values

Radiation dose (d)	w=5 µm	w=10 µm	w=25 µm	w=50 µm
Pre rad	10.3 GHz	20.4 GHz	32.9 GHz	39.6 GHz
200 kRad	9.4 GHz	19.8 GHz	32.5 GHz	39.3 GHz
690 kRad	9.2 GHz	18.4 GHz	29.4 GHz	38.9 GHz
1.3 MRad	8.3 GHz	16.9 GHz	24.3 GHz	36.6 GHz
2 MRad	7.7 GHz	15.7 GHz	20.5 GHz	33.6 GHz
2.7 MRad	7.5 GHz	14.0 GHz	18.9 GHz	28.7 GHz
6.25 MRad	5.5 GHz	8.8 GHz	10.4 GHz	19.9 GHz

5. Conclusion

We present, for the first time, data on the degradation of forward-active small-signal model parameters in bulk NMOS devices due to electron radiation. It is found that model resistances and capacitances tend to increase with d, while g_m reduces across all four irradiated devices. The approach to modelling TID degradation in CMOS devices is shown to produce S-parameter responses comparable to measurement results up to mm-wave frequencies in a 0.35 µm CMOS process, and that the model parameters calculated by regression agree well with those estimated from measured S-parameters. The approach is further used to generate S-parameter responses at 6.25 MRad total dose, thereby illustrating the effect of TID on impedance matching, $|A_i|$, U, f_T and f_{max}. It is found that the predictive modelling approach produces results in line with previous studies.

Future work will extend this approach to compact modelling of CMOS devices, where the effect of TID on biasing conditions and nonlinear responses may be evaluated. The specific extracted model variation expressions will be further validated using a larger number of sample devices (to enable error estimates), as well as evaluated across a wider range of process nodes to see if the results agree qualitatively.

Acknowledgment

The authors wish to thank NUFFIC for supporting this work under the NICHE funding programme which was done under grant number NICHE-ZMB-037 as well as Mr L Netshivhera for performing the reference irradiations using the radiotherapy system and Mr Maxwell Ballot for the assistance rendered in the dose rate verification experiments.

.

References

[1] J. N. Pelton, “New Millimeter, Terahertz, and Light-Wave Frequencies for Satellite Communications,” in *Handbook of Satellite Applications*, Cham: Springer International Publishing, 2017, pp. 413–429.

[2] F. Gianesello *et al.*, “65 nm RFCMOS technologies with bulk and HR SOI substrate for millimeter wave passives and circuits characterized up to 220 GHZ,” in *2006 IEEE MTT-S International Microwave Symposium Digest*, 2006, pp. 1927–1930, doi: 10.1109/MWSYM.2006.249810.

[3] J. D. Cressler and H. A. Mantooth, *Extreme environment electronics*. CRC Press, 2012.

[4] A. Telli and M. Askar, “CMOS LNA design for LEO space S-band applications,” in *CCECE 2003 - Canadian Conference on Electrical and Computer Engineering. Toward a Caring and Humane Technology (Cat. No.03CH37436)*, 2003, vol. 1, pp. 27–30, doi: 10.1109/CCECE.2003.1226336.

[5] T. R. Oldham and F. B. McLean, “Total ionizing dose effects in MOS oxides and devices,” *IEEE Trans. Nucl. Sci.*, vol. 50, no. 3, pp. 483–499, Jun. 2003, doi: 10.1109/TNS.2003.812927.

[6] E. Simoen *et al.*, “Short-channel radiation effect in 60 MeV proton irradiated 0.13 µm CMOS transistors,” *IEEE Trans. Nucl. Sci.*, vol. 50, no. 6, pp. 2426–2432, Dec. 2003, doi:

10.1109/TNS.2003.820612.
[7] M. T. Yang, P. P. C. Ho, Y. J. Wang, T. J. Yeh, and Y. T. Chia, “Broadband small-signal model and parameter extraction for deep sub-micron MOSFETs valid up to 110 GHz,” in *IEEE Radio Frequency Integrated Circuits (RFIC) Symposium, 2003*, 2003, pp. 369–372, doi: 10.1109/RFIC.2003.1213964.
[8] S. N. Ong, K. S. Yeo, K. W. J. Chew, and L. H. K. Chan, “Substrate-Induced Noise Model and Parameter Extraction for High-Frequency Noise Modeling of Sub-Micron MOSFETs,” *IEEE Trans. Microw. Theory Tech.*, vol. 62, no. 9, pp. 1973–1985, Sep. 2014, doi: 10.1109/TMTT.2014.2340375.
[9] H. Escid, M. Attari, M. A. Aidir, and W. Mechti, “0.35 μm CMOS OPTICAL SENSOR FOR AN INTEGRATED TRANSIMPEDANCE CIRCUIT.,” *Int. J. Smart Sens. Intell. Syst.*, vol. 4, no. 3, 2011.
[10] The Radiation Dose Assessment, “External Dose Assessment,” *RADAR-The Decay Data*, 2019. [Online]. Available: http://www.doseinfo-radar.com/RADARDecay.html.
[11] National Institute of Standards and Technology, “ESTAR: Stopping powers and ranges for electrons,” *National institute of stanadards and technology*, 2019. [Online]. Available: https://physics.nist.gov/PhysRefData/Star/Text/ESTAR.html.
[12] S. Venkataraman *et al.*, “Impact of proton irradiation on the RF performance of 0.12/spl mu/m CMOS technology [MOSFET devices],” in *Reliability Physics Symposium, 2005. Proceedings. 43rd Annual. 2005 IEEE International*, 2005, pp. 356–359.
[13] E. B. S. No, “22900,“,” *Total Dose Steady-State Irradiat. Test Method", Eur. Sp. Components Coord. Std*, 2007.
[14] D. Lewis, A. Micke, X. Yu, and M. F. Chan, “An efficient protocol for radiochromic film dosimetry combining calibration and measurement in a single scan,” *Med. Phys.*, vol. 39, no. 10, pp. 6339–6350, 2012.
[15] J. Stenarson and K. Yhland, “A Reformulation and Stability Study of TRL and LRM Using S-Parameters,” *IEEE Trans. Microw. Theory Tech.*, vol. 57, no. 11, pp. 2800–2807, Nov. 2009, doi: 10.1109/TMTT.2009.2032481.
[16] I. S. Esqueda, *Modeling of total ionizing dose effects in advanced complementary metal-oxide-semiconductor technologies*. Arizona State University, 2011.
[17] L. W. Massengill, “Radiation Effects in Si CMOS Platforms,” in *Extreme Environment Electronics*, CRC Press, 2012, pp. 155–174.
[18] J. A. De Lima, M. A. G. Silveira, K. H. Cirne, R. B. B. Santos, and N. H. Medina, “X-ray radiation effects in Overlapping Circular-Gate MOSFET’s,” in *2011 12th European Conference on Radiation and Its Effects on Components and Systems*, 2011, pp. 88–91, doi: 10.1109/RADECS.2011.6131374.
[19] Y. Li *et al.*, “Study of γ-ray irradiation influence on TiN/HfO2/Si MOS capacitor by C-V and DLTS,” *Superlattices Microstruct.*, vol. 120, pp. 313–318, Aug. 2018, doi: 10.1016/j.spmi.2018.05.046.

Figures

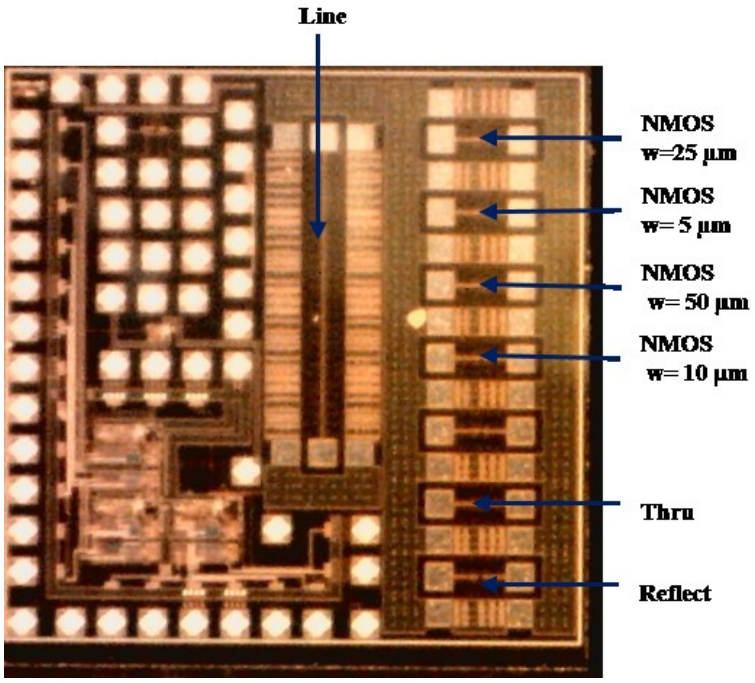

Fig. 1: Die micrograph indicating devices and on-wafer calibration standards.

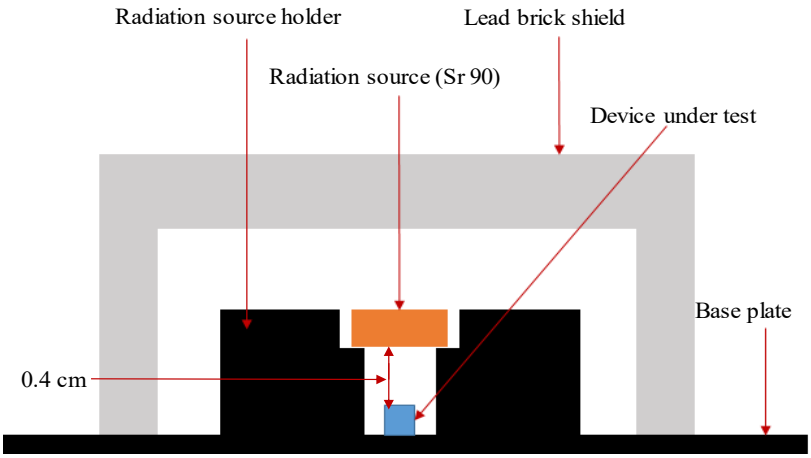

Fig. 2(a): Radiation experiment setup

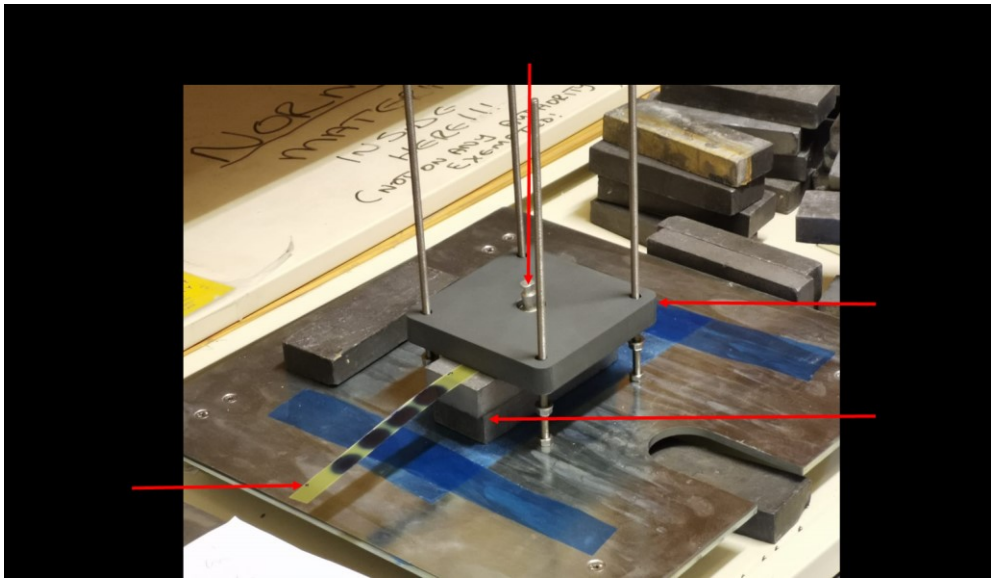

Fig. 2(b): Radiation experiment for verification of dose rate

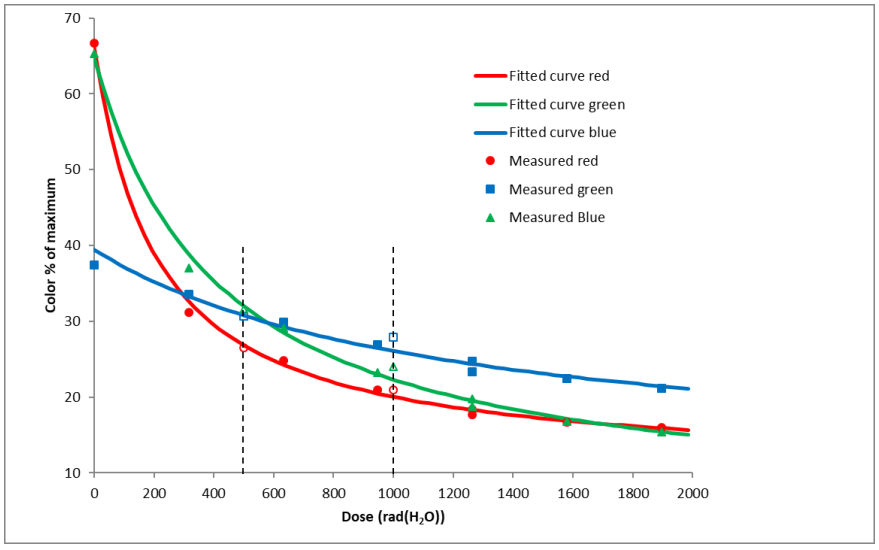

Fig. 2(c): Gafchromic calibration curves for the Sr-90 source. The open symbols (emphasized by dashed lines) show reference doses given by a radiotherapy machine.

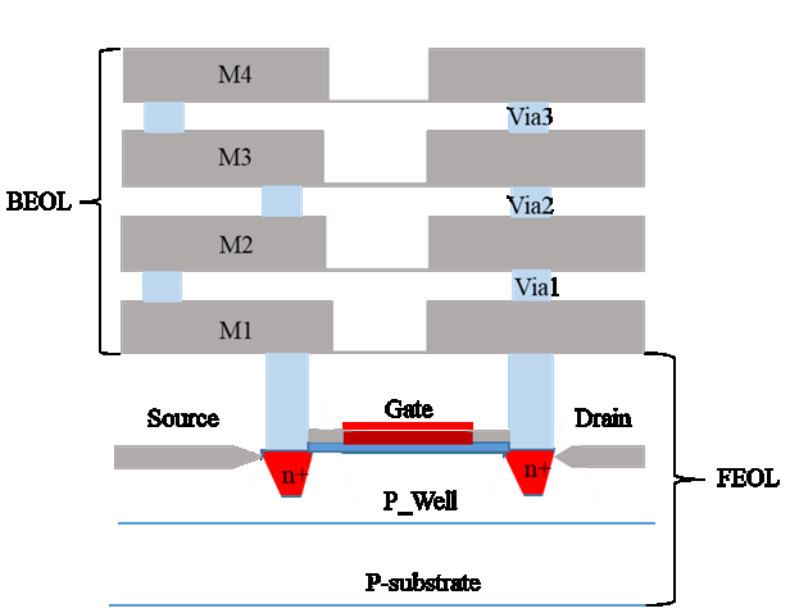

Fig.3(a) : Cross section of the NMOS device with layers of the C35 process stack-up

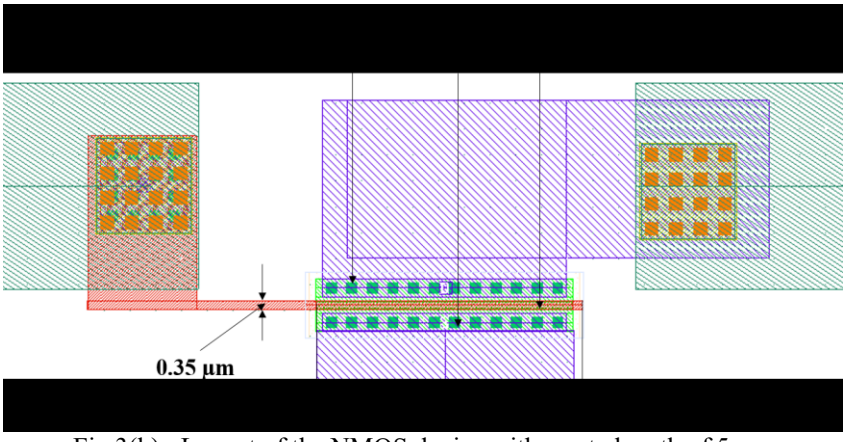

Fig 3(b) : Layout of the NMOS device with a gate length of 5 µm

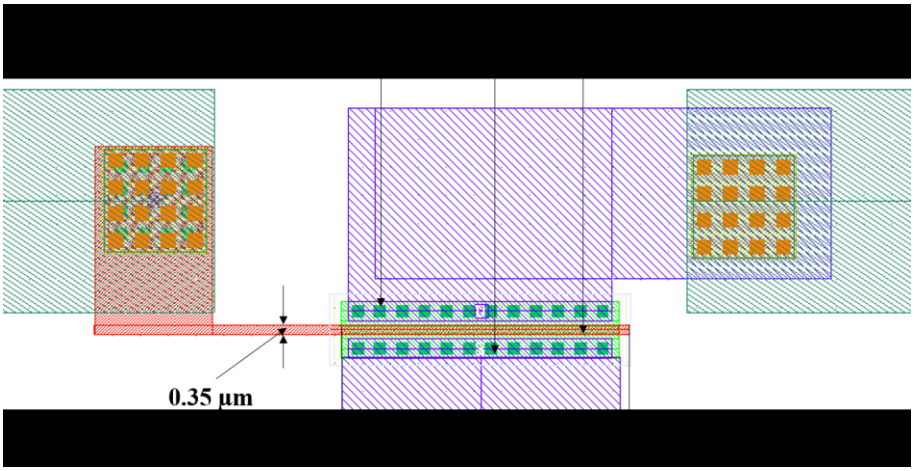

Fig 3(c) : Layout of the NMOS device with a gate length of 10 µm

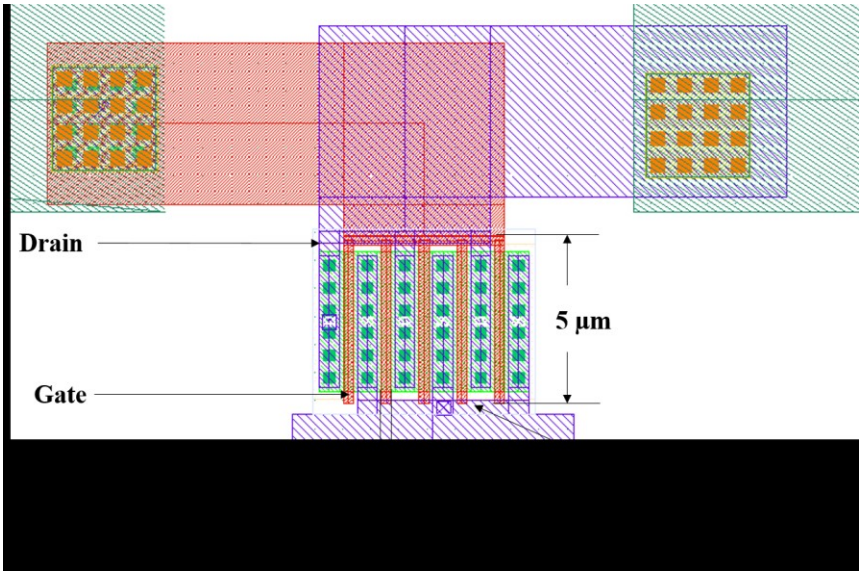

Fig 3(d) : Layout of the NMOS device with total gate length of 25 µm

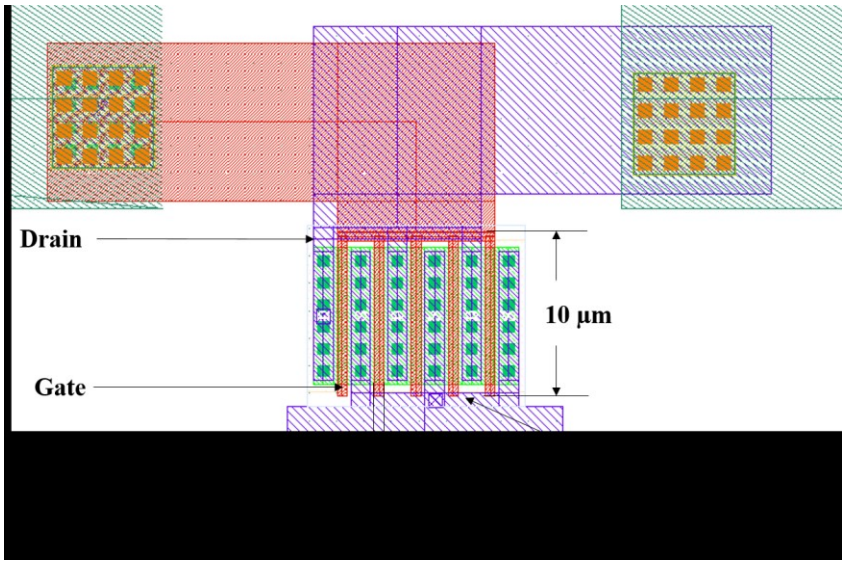

Fig 3(e): Layout of the NMOS device with total gate length of 50 µm

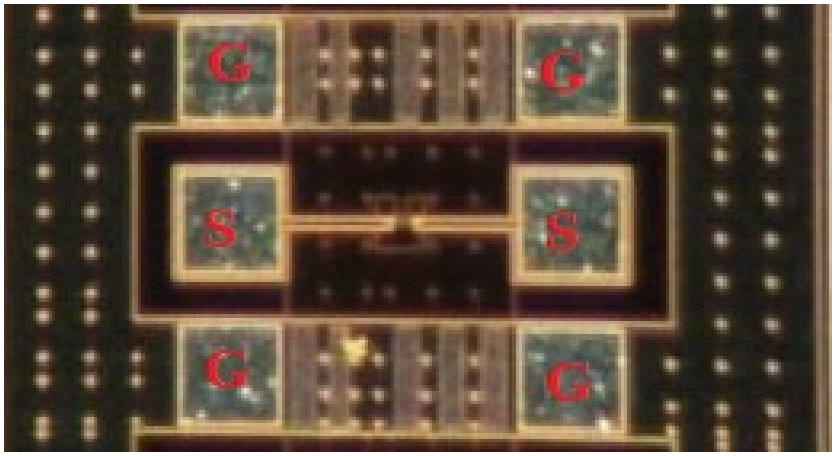

Fig 3(f) : Layout of the NMOS devices under test.

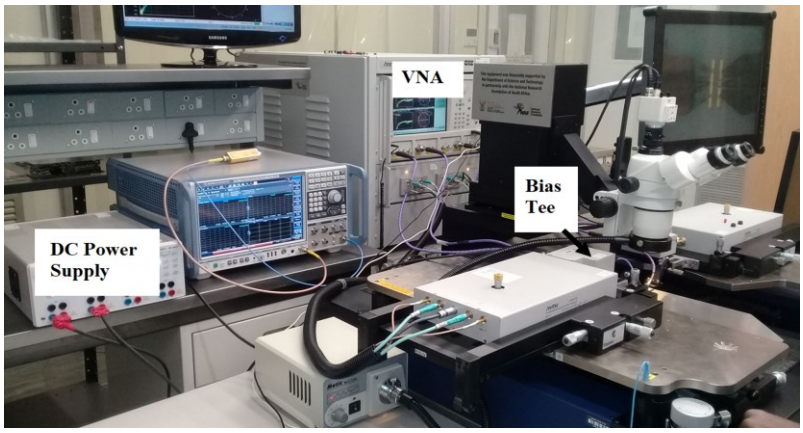

Fig. 4. Photo of the setup for S-parameter measurements in the cleanroom.

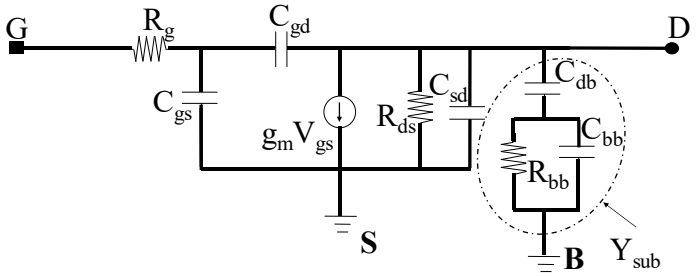

Fig. 5. Small-signal model for MOSFET, adapted from [8].

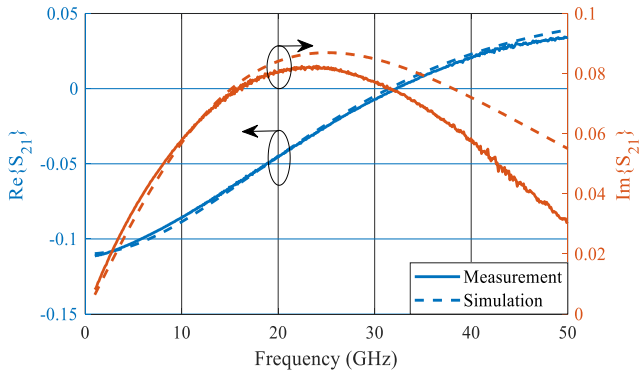

Fig. 6. Comparison of S_{21} for extracted model to measurement for w = 5 µm

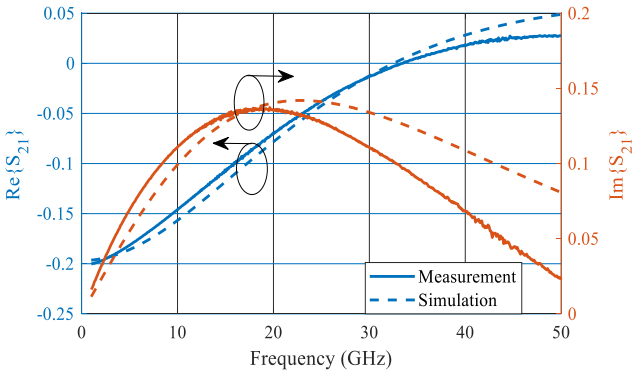

Fig. 7. Comparison of S_{21} for extracted model to measurement for w = 10 µm

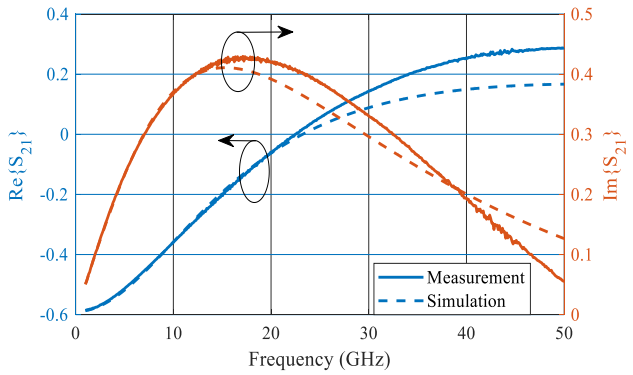

Fig. 8. Comparison of S_{21} for extracted model to measurement for w = 25 µm

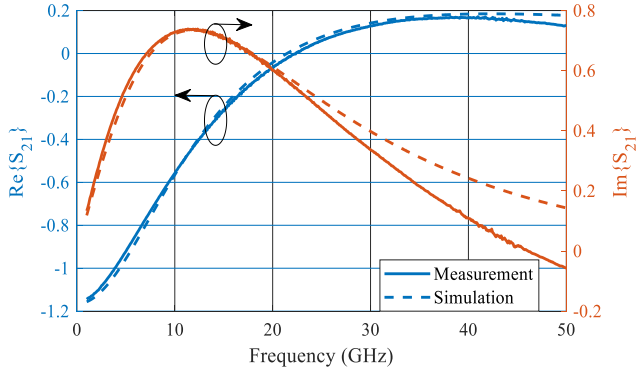

Fig. 9. Comparison of S_{21} for extracted model to measurement for w=50 µm

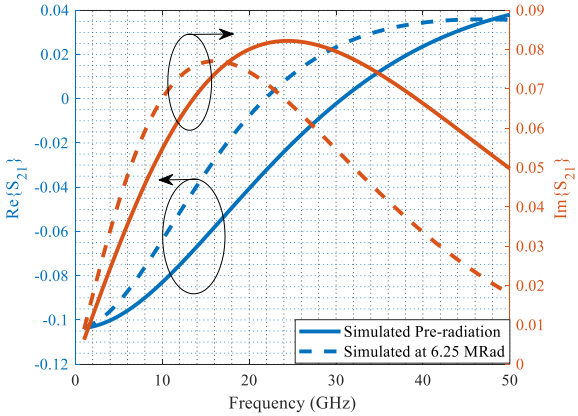

Fig. 10. S_{21} for NMOS device with gate width of 5 µm at two *d* values

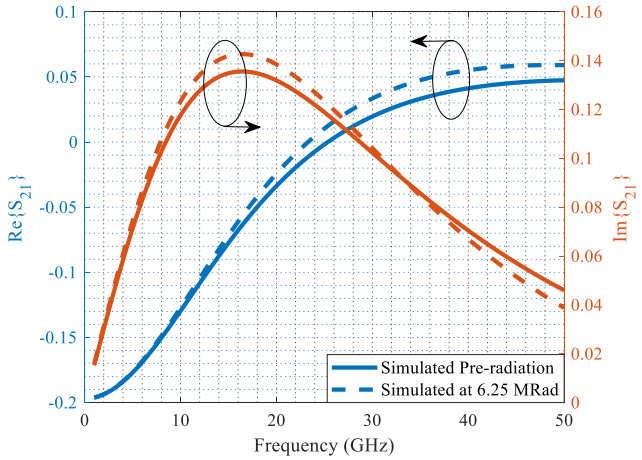

Fig. 11. S_{21} for NMOS device with gate width of 10 µm at two *d* values

Fig. 12. S_{21} for NMOS device with gate width of 25 µm at two *d* values

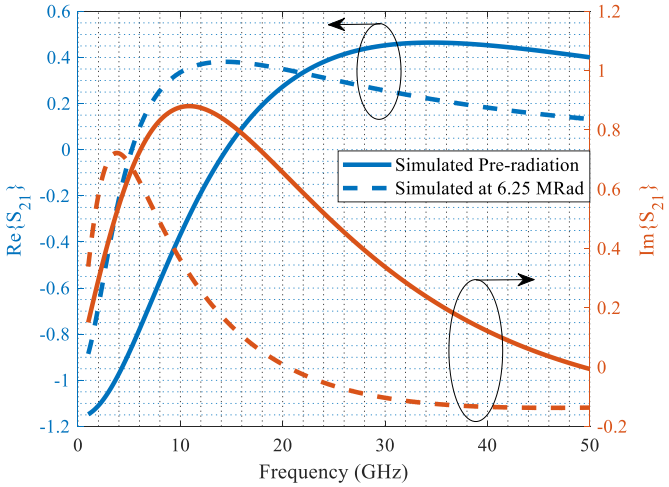

Fig. 13. S_{21} for NMOS device with gate width of 50 µm at two *d* values

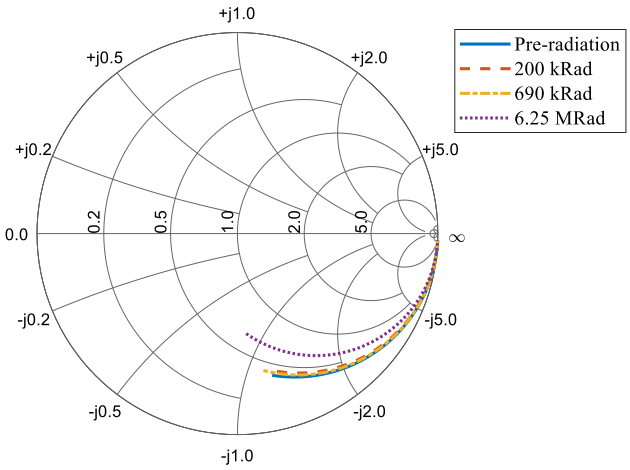

Fig. 14. Smith chart for S_{11} for NMOS with gate width of 5 µm

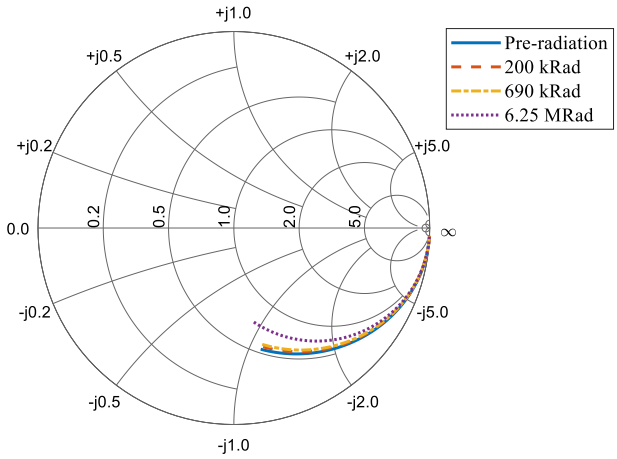

Fig. 15. Smith chart for S_{11} for NMOS with gate width of 10 µm

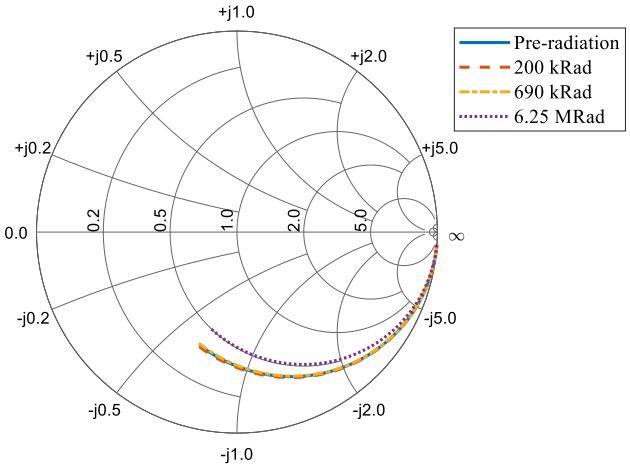

Fig. 16. Smith chart for S_{11} for NMOS with gate width of 25 µm

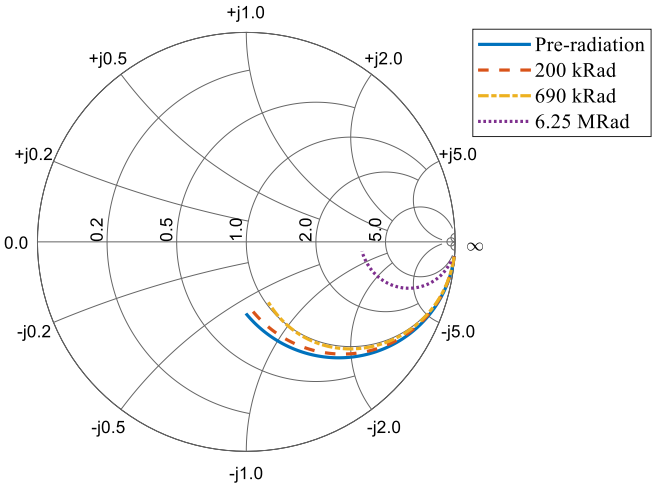

Fig. 17. Smith chart for S_{11} for NMOS with gate width of 50 µm

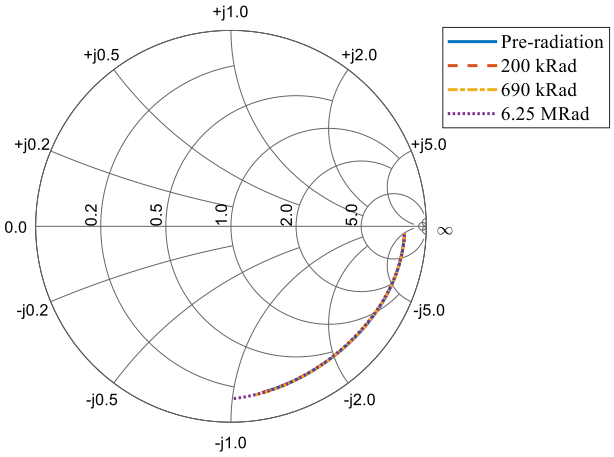

Fig. 18. Smith chart for S_{22} for NMOS with gate width of 5 µm

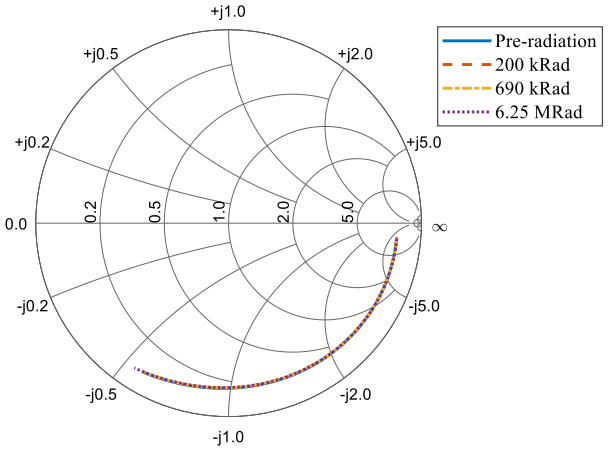

Fig. 19. Smith chart for S_{22} for NMOS with gate width of 10 µm

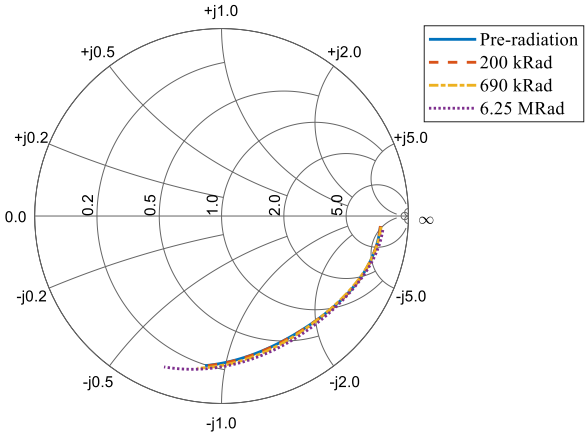

Fig. 20. Smith chart for S_{22} for NMOS with gate width of 25 µm

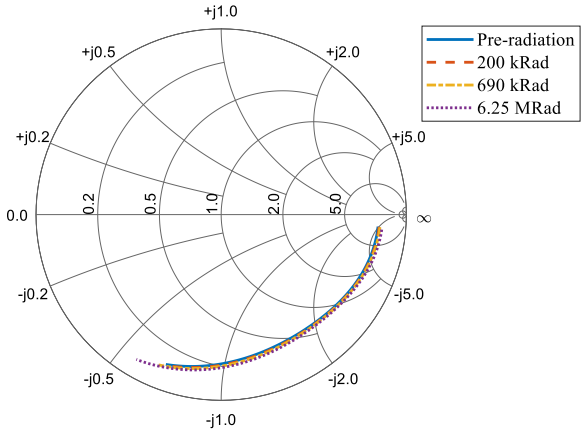

Fig. 21. Smith chart for S_{22} for NMOS with gate width of 50 µm

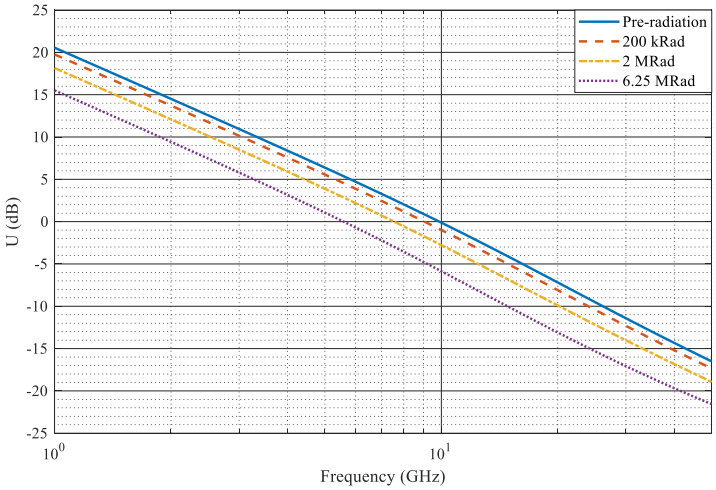

Fig. 22: Unilateral gain for NMOS device with gate width of 5 µm

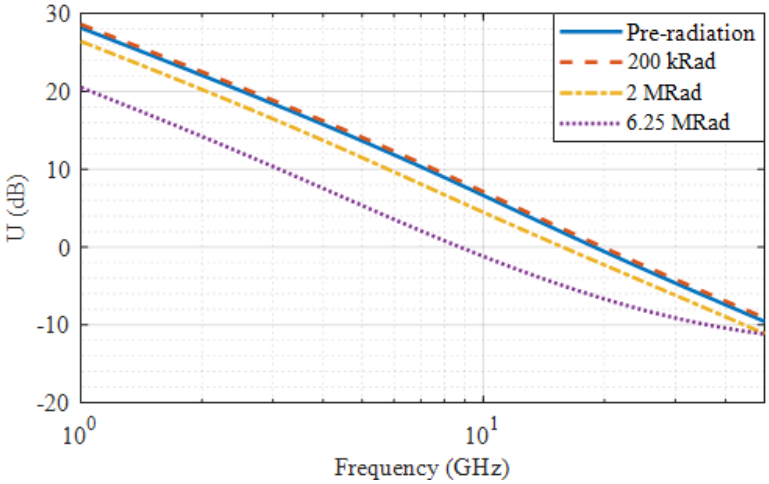

Fig. 23: Unilateral gain for NMOS device with gate width of 10 µm

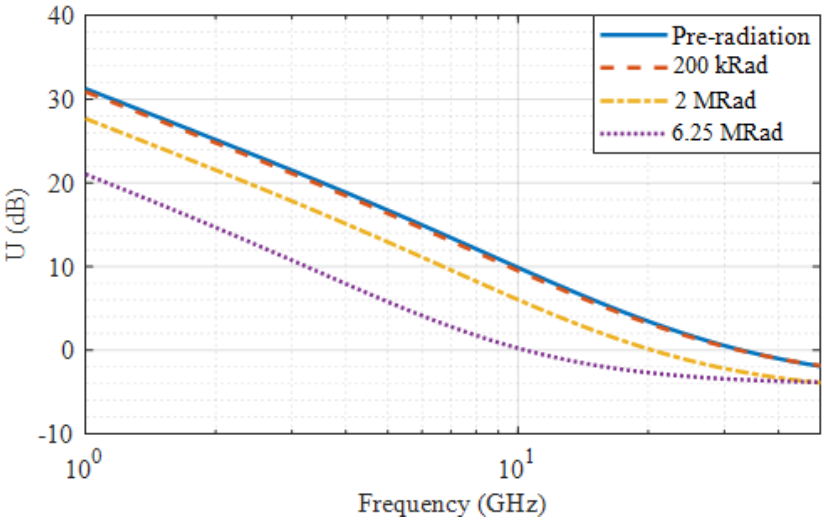

Fig. 24: Unilateral gain for NMOS device with gate width of 25 µm

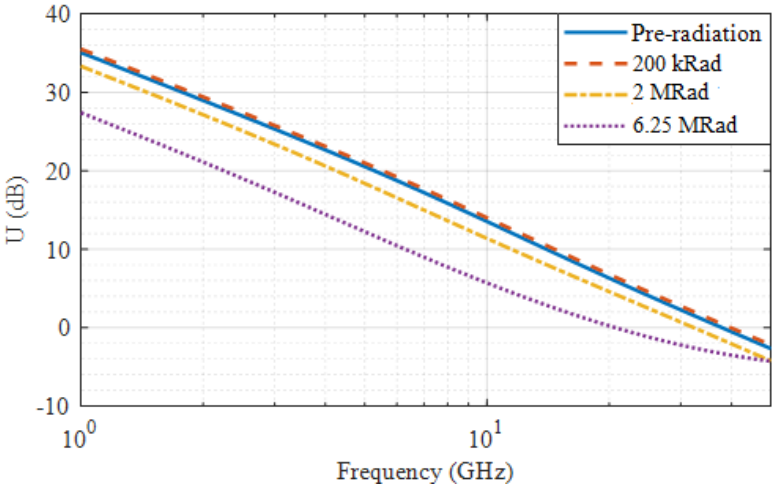

Fig. 25: Unilateral gain for NMOS device with gate width of 50 µm

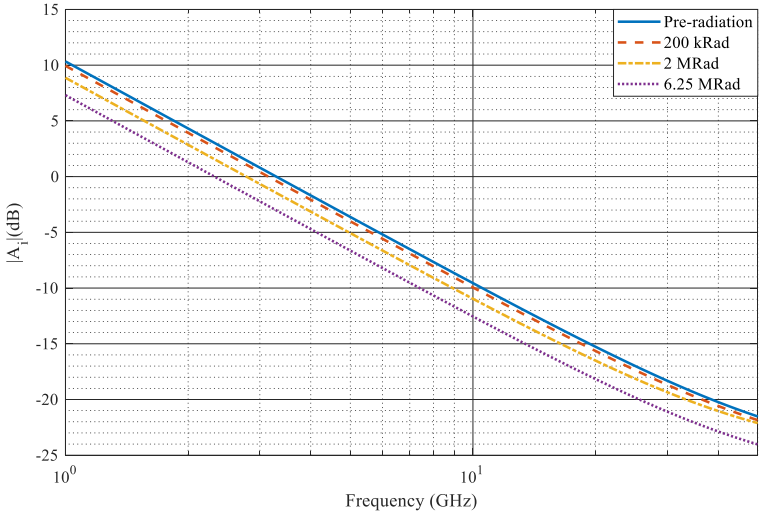

Fig. 26. $|A_i|$ at various *d* values for NMOS device with gate width of 5 µm

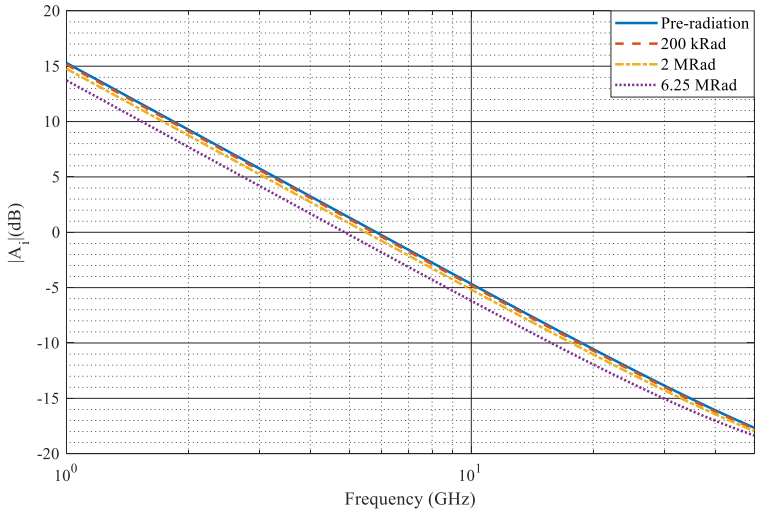

Fig. 27. $|A_i|$ at various *d* values for NMOS device with gate width of 10 µm

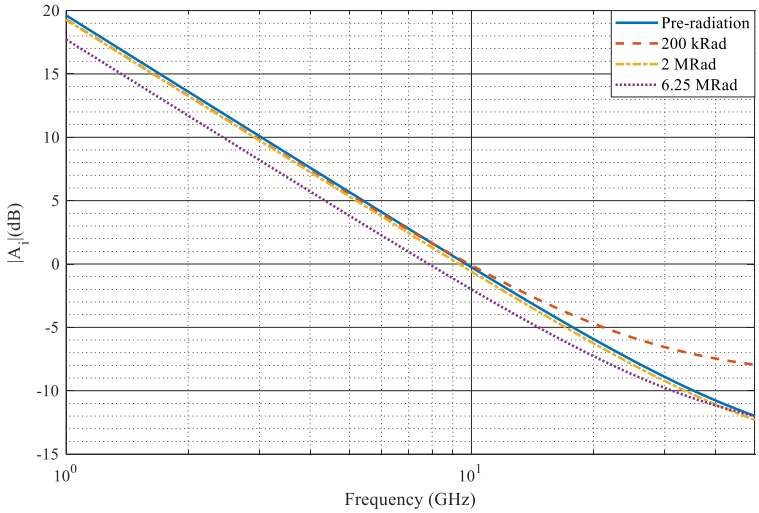

Fig. 28. $|A_i|$ at various *d* values for NMOS device with gate width of 25 µm

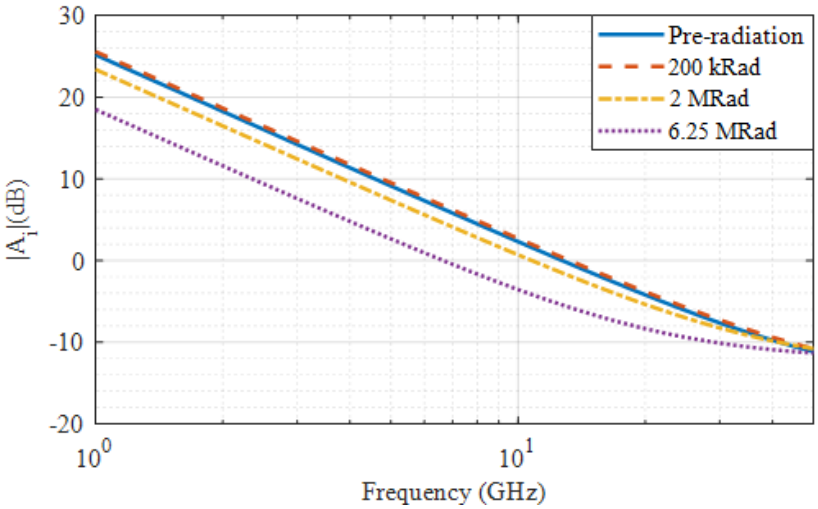

Fig. 29. $|A_i|$ at various *d* values for NMOS device with gate width of 50 µm